


 Cite this: *RSC Adv.*, 2025, **15**, 45026

Synthesis, optical characterization, and antimicrobial applications of gold-coated $\text{Gd}_2\text{O}_3:\text{Eu}^{3+}$ nanostructures

Nguyen Thanh Huong, ^a Pham Thi Lien, ^a Hoang Thi Khuyen, ^a Nguyen Thi Ngoc Anh, ^a Do Khanh Tung, ^a Nguyen Vu, ^a Lam Thi Kieu Giang, ^a Dinh Manh Tien^a and Nguyen Thanh Binh^b

This study reports the synthesis and characterization of Eu^{3+} -doped gadolinium oxide ($\text{Gd}_2\text{O}_3:\text{Eu}^{3+}$) nanomaterials and their surface-modified counterparts coated with gold nanoparticles (Au NPs). A comprehensive suite of techniques, including thermogravimetric analysis (TGA), field-emission scanning electron microscopy (FESEM), high-resolution transmission electron microscopy (HRTEM), UV-Vis absorption spectroscopy, zeta potential measurements, X-ray diffraction (XRD), Raman spectroscopy, and photoluminescence were used to analysis and evaluate the synthesized samples. The SEM, TEM and XRD results revealed the successful formation of cubic-phase $\text{Gd}_2\text{O}_3:\text{Eu}^{3+}$ with uniform spherical morphology (~ 80 nm) and the homogeneous deposition of sub 10 nm Au NPs on their surfaces. The photoluminescence spectra clearly displayed the characteristic Eu^{3+} emission transitions (${}^5\text{D}_0 \rightarrow {}^7\text{F}_j$, $j = 0-4$), confirming effective doping. The introduction of Au NPs induced a surface plasmon resonance effect, which significantly enhanced the antibacterial efficacy of the nanocomposite. This was quantitatively demonstrated against a panel of clinically relevant Gram-negative and Gram-positive bacterial strains, as well as the fungal pathogen *Candida albicans* (*Escherichia coli* ATCC 25922, *Staphylococcus aureus* ATCC 25923, *Klebsiella pneumoniae* ATCC 70060, *Pseudomonas aeruginosa* ATCC 27853, and *Candida albicans* ATCC 14053). The Au-coated $\text{Gd}_2\text{O}_3:\text{Eu}^{3+}$ samples exhibited significantly enhanced bactericidal efficiency compared to the uncoated ones. Our findings underscore the strategic advantages of coupling lanthanide luminescence with noble metal plasmonics, paving the way for a novel class of multifunctional nanomaterials with potent applications in antimicrobial therapy and biomedical diagnostics.

Received 1st October 2025
 Accepted 13th November 2025

DOI: 10.1039/d5ra07449e
rsc.li/rsc-advances

1 Introduction

Rare-earth-dope metal oxides represent a cornerstone of modern functional materials, with europium-doped gadolinium oxide ($\text{Gd}_2\text{O}_3:\text{Eu}^{3+}$) standing out due to its exceptional luminescent properties. The Eu^{3+} ion serves as the primary emission center with characteristic red emission bands (${}^5\text{D}_0 \rightarrow {}^7\text{F}_j$).¹⁻⁶ The Gd_2O_3 host matrix is highly valued for its thermal stability, chemical inertness, and wide bandgap, which makes it particularly suitable for efficient energy transfer to the dopant Eu^{3+} ions.^{7,8} At the nanoscale, $\text{Gd}_2\text{O}_3:\text{Eu}^{3+}$ NPs exhibit strong luminescence intensity with high photostability, and their optical properties can be finely tuned through morphology control and dopant concentration.⁹⁻¹¹ These attributed propelled their use in diverse applications, including as: (i)

phosphors in LEDs and displays; (ii) fluorescent probes in biosensing and bioimaging; (iii) fluorescent labels in biomedical applications due to their biocompatibility and sensitivity for trace-level detection.¹²⁻¹⁶

To further augment the functionality of these luminescent nanomaterials, the integration of plasmonic components has emerged as a powerful strategy. Decorating $\text{Gd}_2\text{O}_3:\text{Eu}^{3+}$ NPs with gold (Au) NPs introduces a localized surface plasmon resonance (LSPR) effect. This LSPR can significantly amplify the local electromagnetic field around the NPs,^{17,18} which has the potential to enhance the excitation rate and modify the emission properties of the adjacent Eu^{3+} ions.^{19,20} Beyond optical modulation, Au NPs contribute their own unique biophycochemical properties, including strong optical absorption and scattering, and well documented antimicrobial activity.^{21,22} The biocidal mechanism of Au NPs is multifaceted, involving their attachment to microbial cell walls, which can disrupt membrane potential and permeability, interfere with vital metabolic processes, and inactivate essential enzymes, ultimately leading to microbial cell and bacteria death.

^aInstitute of Materials Sciences, Vietnam Academy of Science and Technology, 18 Hoang Quoc Viet, Nghia Do, Hanoi, Vietnam. E-mail: nthuong@ims.vast.ac.vn

^bInstitute of Physics, Vietnam Academy of Science and Technology, 10 Dao Tan, Hanoi, Vietnam

Conventional nanomaterials employed for antimicrobial applications present significant trade-offs. While Ag-based nanomaterials exhibit high intrinsic bactericidal efficacy, their widespread use is frequency constrained by concerns over poor stability in biological media and dose-dependent cytotoxicity.²¹ Similarly, photocatalytic agents like TiO₂ and ZnO are promising but typically require energy-intensive UV or specific high-energy visible-light excitation for their activity.^{21,23} In contrast, the Gd₂O₃:Eu³⁺/Au hybrid developed here integrates stable red emission, plasmon-enhanced antibacterial activity, and biointerface potential. These multifunctional properties arise from the robust and biocompatible Gd₂O₃ matrix coupled with the LSPR effect of Au nanoparticles,^{17,18,23} offering a simple yet effective alternative to conventional antibacterial materials.

The convergence of lanthanide luminescence and gold plasmonic thus create a novel multifunctional platform. Such a system synergistically combines the capabilities of a trackable optical label with the inherent antimicrobial action of its constituent materials. This opens avenues for developing “theragnostic” agents capable of simultaneous diagnosis and treatment. Potential applications are vast, including (i) light-activated antibacterial water purification systems; (ii) self-sanitizing medical antimicrobial surfaces; (iii) smart biosensors that can not only detect but also neutralize pathogenic microorganisms.

While the plasmon-enhanced optical properties of similar systems have been explored, a comprehensive biophysical study correlating their structural and photonic characteristics with their antimicrobial efficacy against a broad spectrum of clinically relevant pathogens remains less developed. Herein, we report the synthesis and detailed characterization of both Gd₂O₃:Eu³⁺ and Au-coated Gd₂O₃:Eu³⁺ nanomaterials. We systematically investigated their structural, colloidal and optical properties, and critically evaluated their antibacterial performance against a panel of five representative microbial strains: *Escherichia coli* (ATCC 25922), *Staphylococcus aureus* (ATCC 25923), *Klebsiella pneumoniae* (ATCC 70060), *Pseudomonas aeruginosa* (ATCC 27853), and the fungal pathogen *Candida albicans* (ATCC 14053). This work aims to establish a clear

structure–property–activity relationship for these hybrid (composite) nanostructures, highlighting their significant potential for advanced biomedical and antimicrobial applications.

2 Experimental

2.1 Materials

All chemicals used in the synthesis were high-purity reagents: gadolinium(III) nitrate hexahydrate (Gd(NO₃)₃·6H₂O, 99.99%); europium(III) nitrate pentahydrate (Eu(NO₃)₃·5H₂O, 99.99%); gold(III) chloride trihydrate (HAuCl₄·3H₂O, 99.9%); polyethylenimine ((C₂H₅N)_n, 37 wt.% in H₂O), phosphate-buffered saline (PBS, pH 7.4) were purchased from Sigma-Aldrich; trisodium citrate dihydrate (C₆H₅Na₃O₇·2H₂O), urea (CO(NH₂)₂ powder, 99.9%); ethanol (C₂H₅OH, ≥99.8%) was obtained from Merck. All synthesis procedures were carried out using deionized (DI) water.

2.2 Experimental

2.2.1 Synthesis of Gd₂O₃:Eu³⁺ material. The Gd₂O₃:Eu³⁺ nanomaterial was synthesized *via* a wet-chemical and subsequent calcination method (Fig. 1). First, a precursor solution was prepared by mixing aqueous solution of Eu(NO₃)₃ (0.05 M) and Gd(NO₃)₃ (0.05 M) to achieve a [Eu³⁺]/[Gd³⁺] molar ratio of 5%, following by stirring for 30 min. Subsequently, this metal precursor solution was then added dropwise into 150 ml of a 0.8 M urea solution (0.8 M) contained in a reaction flask under constant stirring. The resulting mixture was stirred for 2 h at room temperature, then heated to 85 °C and maintained at this temperature for 1 h to facilitate precipitation before rapidly cooled in room temperature. The obtained product was collected by centrifugation and washed sequentially with DI water and ethanol (twice each) at 5500 rpm. The purified product was dried at 70 °C for 24 h, yielding the intermediate compound Eu³⁺-doped gadolinium carbonate hydrate (Gd(OH)CO₃·H₂O/Eu³⁺). The final high-purity Gd₂O₃:Eu³⁺ powder was obtained by calcining this intermediate in a muffle furnace at 700 °C for 5 h to remove volatile components and organic

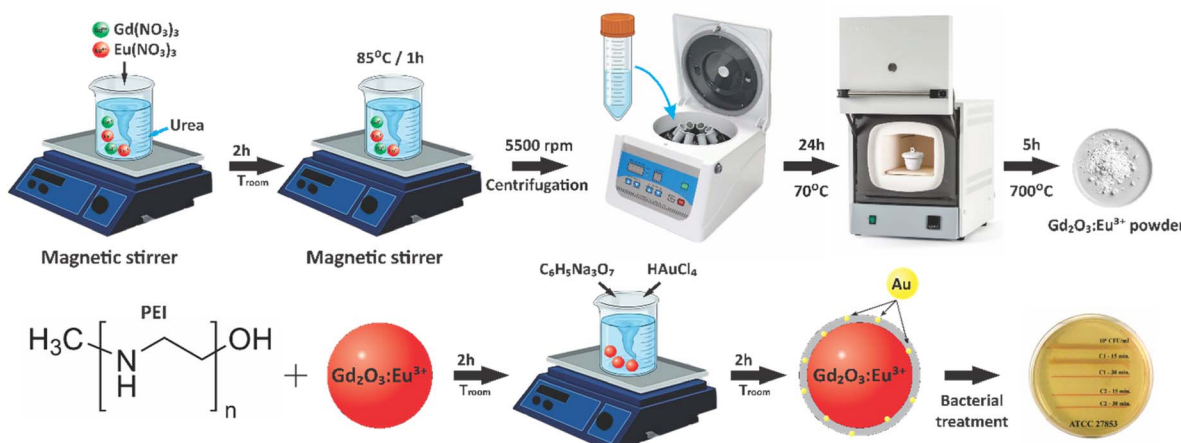


Fig. 1 Schematic diagram of synthesis process of Gd₂O₃:Eu³⁺/Au *via* a wet-chemical and subsequent calcination method.



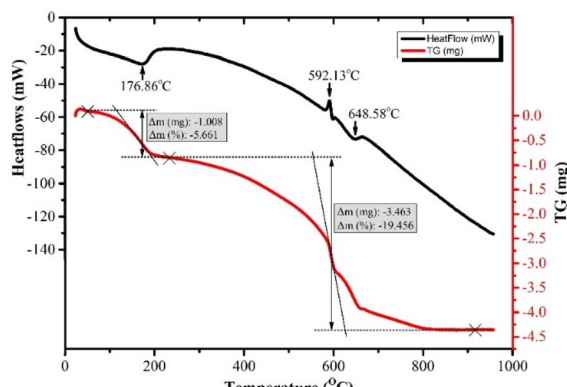


Fig. 2 TG and DTG of $\text{Gd}(\text{OH})\text{CO}_3 \cdot \text{H}_2\text{O}:\text{Eu}^{3+}$ sample.

residues in order to ensure complete decomposition and crystallization.

2.2.2 Synthesis of $\text{Gd}_2\text{O}_3:\text{Eu}^{3+}/\text{Au}$ material. The $\text{Gd}_2\text{O}_3:\text{Eu}^{3+}/\text{Au}$ nanocomposite was synthesized *via* an *in situ* reduction method. Briefly, 200 mg of as-synthesized $\text{Gd}_2\text{O}_3:\text{Eu}^{3+}$ powder was dispersed in 20 ml of DI water *vis* ultrasonication and vortex mixing for 2 h. To functionalize the surface, 100 μl PEI was added, and the mixture was agitated for an additional 2 h. The resulting suspension was then transferred into a 100 ml round-bottom flask, and 1 ml of an aqueous HAuCl_4 solution (0.25 M) was introduced under constant stirring. The mixture was stirred and heated to 80 °C, at which point 2 ml of a tri-sodium citrate dihydrate solution ($\text{C}_6\text{H}_5\text{Na}_3\text{O}_7 \cdot 2\text{H}_2\text{O}$) was added dropwise. The reaction was maintained at 80 °C for 30 min to ensure complete NPs growth. Upon cessation of heating, the mixture cooled to room temperature with continuous stirring. The final product was collected by centrifugation, washed sequentially with DI water and phosphate-buffered saline (PBS), and ultimately redispersed in PBS for storage at 4 °C to antibacterial testing.

2.2.3 Application of $\text{Gd}_2\text{O}_3:\text{Eu}^{3+}/\text{Au}$ material in bacterial treatment

2.2.3.1 Bacterial strains used in the study. The antimicrobial efficacy of the synthesized nanomaterials was assessed against five relevant microbial strains, selected to represent a diverse range of pathogenic structure and resistance mechanisms, including the Gram-negative bacteria *Escherichia coli* ATCC

25922, *Klebsiella pneumoniae* ATCC 700603, *Pseudomonas aeruginosa* ATCC 27853; Gram-positive bacteria *Staphylococcus aureus* ATCC 25923; and the pathogenic yeast *Candida albicans* ATCC 14053. All strains are standard reference organisms recommended by the Clinical and Laboratory Standards Institute (CLSI), a selection that ensured the methodological rigor, reproducibility, and a clinical comparability of the obtained results.

2.2.3.2 Bacterial treatment procedure. The antibacterial activity of the synthesized nanomaterials was evaluated against the five reference strains using a streak plate method. Two sample solutions were tested: C1, a suspension of $\text{Gd}_2\text{O}_3:\text{Eu}^{3+}$ (10 mg ml^{-1}) and C2, a suspension of $\text{Gd}_2\text{O}_3:\text{Eu}^{3+}/\text{Au}$ (10 mg ml^{-1}). Microbial suspensions were standardized to a concentration of 10^6 CFU ml^{-1} in sterile saline for *Escherichia coli* ATCC 25922, *Staphylococcus aureus* ATCC 25923, *Klebsiella pneumoniae* ATCC 700603, *Pseudomonas aeruginosa* ATCC 27853, and *Candida albicans* ATCC 14053. For the assay, 100 μl of each sample (C1 or C2) was combined with 100 μl of the prepared microbial suspension in an individual sterile well. After mixing thoroughly, the mixtures were incubated for two exposure times (15 min and 30 min). For each interval, a 10 μl aliquot was collected and streaked onto the appropriate solid agar media: Blood Agar, Uri Agar, and Mueller–Hinton. The plates were then incubated, and the resulting bacterial growth along the streak lines was compared to a control (10^6 CFU ml^{-1} suspension mixed with PBS) to determine and evaluate the bactericidal efficiency of C1 and C2.

2.3 Characterization of material and measurement

The structural and optical properties of the synthesized nanomaterials were characterized using a suite of analytical techniques. The crystal phase was determined by X-ray diffraction (XRD, Bruker D8 ADVANCE). Morphological analysis, including particle size and shape, was investigated using field-emission scanning electron microscopy (FESEM, Hitachi S4800) and high-resolution transmission electron microscopy (HRTEM, JEM-2100 JEOL). Thermal stability was assessed *via* thermogravimetric-differential thermal analysis (TG-DTA) on a Labsys evo 1600 system. Fourier Transform Infrared (FTIR) spectroscopy was performed on a Jasco FT/IR-6700 instrument (Jasco International, Japan). The optical characteristics were probed by UV-Vis absorption spectroscopy using a double-beam

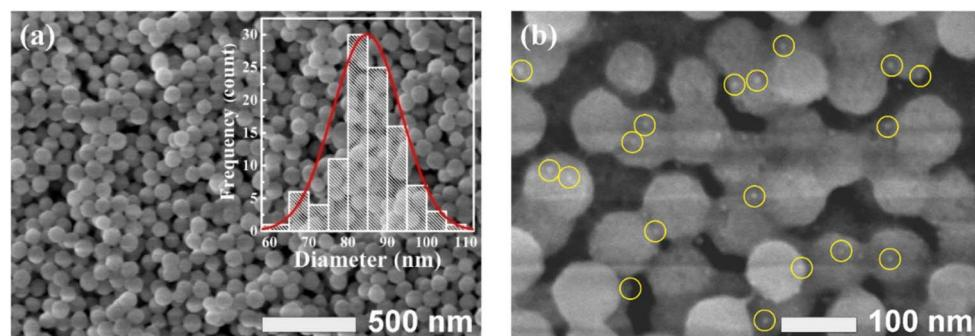


Fig. 3 FESEM images of $\text{Gd}_2\text{O}_3:\text{Eu}^{3+}$ (a) and $\text{Gd}_2\text{O}_3:\text{Eu}^{3+}/\text{Au}$ (b).



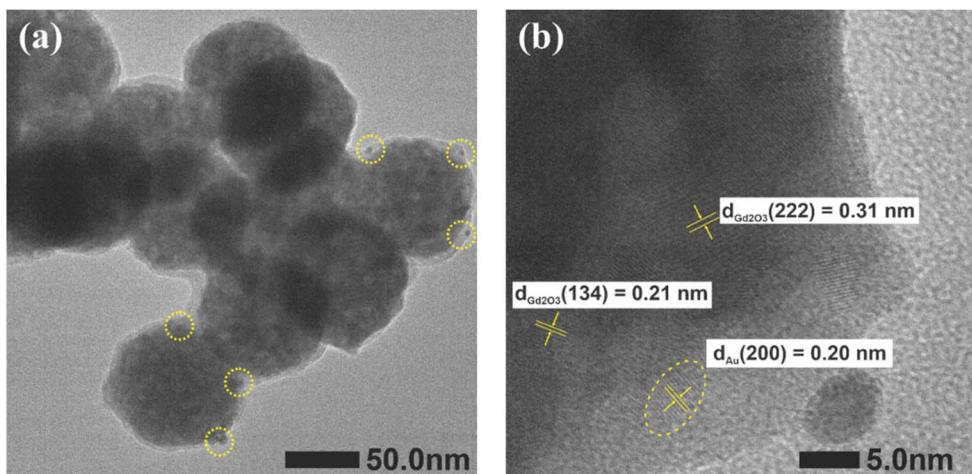


Fig. 4 TEM (a) and HRTEM (b) images of $\text{Gd}_2\text{O}_3:\text{Eu}^{3+}/\text{Au}$ sample.

spectrophotometer, Raman spectroscopy (Horiba XploRA PLUS Raman microscope), Photoluminescence spectroscopy (Horiba Fluorolog-3 spectrofluorometer) and the fluorescence lifetime measurements were carried out using an FLS1000 Photoluminescence Spectrometer (Edinburgh Instruments, UK). Furthermore, the colloidal stability of the NPs in suspension was evaluated by Zeta potential measurements using a Zetasizer Nano ZS (Malvern, UK).

3 Results and discussion

3.1 TGA analysis

Thermogravimetric analysis (TGA) was employed to investigate the effect of temperature on the structural and mass changes of the $\text{Gd}(\text{OH})\text{CO}_3 \cdot \text{H}_2\text{O}/\text{Eu}^{3+}$ precursor and to determine the optimal calcination temperature. As illustrated in Fig. 2, the TGA/DTG profiles reveal a two-stage decomposition process. The first (initial) stage, exhibiting a minor mass loss of

approximately 5.66% with a concomitant endothermic peak at 176.9 °C, is ascribed to the elimination of physisorbed and crystalline water molecules. The second stage, between 250 and 650 °C, more substantial mass loss of about 19.46% occurred, which is associated with prominent DTG peaks at 592.1 °C and 648.6 °C. This stage is mainly attributed to the dehydroxylation and decarboxylation of the precursor, leading to the release of CO_2 and H_2O gases. The subsequent stabilization of the mass beyond 650 °C indicating the completion of decomposition process and the formation of thermally stable $\text{Gd}_2\text{O}_3:\text{Eu}^{3+}$ signifies the complete conversion to the final, beyond this temperature range.

Based on this thermal profile, a calcination temperature of 700 °C was selected to guarantee complete decomposition while preventing premature sintering. The TGA data thus provide clear evidence of the sequential transformation from the metastable hydrated carbonate intermediate to the stable crystalline oxide $\text{Gd}_2\text{O}_3:\text{Eu}^{3+}$ phase. This confirms that the

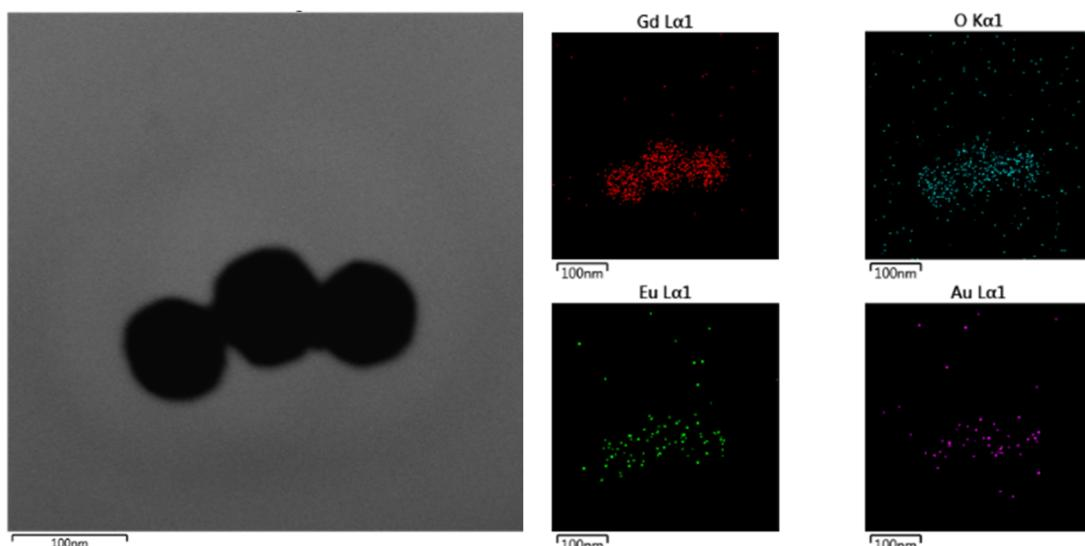


Fig. 5 Mapping of $\text{Gd}_2\text{O}_3:\text{Eu}^{3+}/\text{Au}$ material.



calcination step is critical for producing a high crystalline $\text{Gd}_2\text{O}_3:\text{Eu}^{3+}$ with high thermal stability for its subsequent optical functionality and potential biomedical uses.

3.2 Morphology characterizations

FESEM and HRTEM analyses were employed to characterize the morphology of the synthesized $\text{Gd}_2\text{O}_3:\text{Eu}^{3+}$ and Au-coated $\text{Gd}_2\text{O}_3:\text{Eu}^{3+}$ nanomaterials after calcination at 700 °C. As shown in Fig. 3a, the pristine $\text{Gd}_2\text{O}_3:\text{Eu}^{3+}$ consisted of uniform, spherical particles with smooth surfaces and an average diameter of approximately 80 nm. Following the Au deposition (Fig. 3b) shows numerous smaller Au NPs (<10 nm) uniformly decorated on the surface of the $\text{Gd}_2\text{O}_3:\text{Eu}^{3+}$ spheres. This Au functionalization did not disrupt the overall morphology of the host matrix but successfully created a heterostructure with intimate interfacial contact between Au and the oxide host matrix, as unequivocally by HRTEM (Fig. 4). This well-dispersed, nanoscale architecture of Au NPs on the oxide surface is critical, as it is expected to enhance both light-matter interactions and facilitate the antimicrobial efficacy of the composite material.

HRTEM analysis provides nanoscale structural insight into the Au-coated $\text{Gd}_2\text{O}_3:\text{Eu}^{3+}$ nanocomposites. As shown in Fig. 4a, the low-magnification image confirms the spherical morphology of $\text{Gd}_2\text{O}_3:\text{Eu}^{3+}$ host particle (~80 nm) and reveals an uniform distribution of Au NPs anchored to their surface *via* a thin polymer interlayer. The high-resolution image in Fig. 4b reveals well-defined lattice fringes, enabling crystallographic identification. Measured interplanar spacings of 0.31 nm and 0.21 nm are assigned to the (222) and (134) planes of cubic Gd_2O_3 , respectively, while a spacing of 0.20 nm corresponds to the (200) plane of fcc Au. These *d*-spacings show excellent agreement with the XRD data, providing complementary evidence for the co-existence of both highly crystalline phases, the cubic structure of Gd_2O_3 and fcc Au.

The sharp lattice fringes and absence of amorphous regions further confirm the high crystallinity and structural integrity of the synthesized hetero structure with no detectable impurities or structural distortions.

Energy-dispersive X-ray spectroscopy (EDS) elemental mapping (Fig. 5) confirms homogeneous distribution of the constituent elements – Gd, O, Eu, and Au – within the $\text{Gd}_2\text{O}_3:\text{Eu}^{3+}$ /Au nanocomposite. The successful and uniform decoration of Au NPs without disrupting the host $\text{Gd}_2\text{O}_3:\text{Eu}^{3+}$ matrix, signifies the formation of a stable core-shell heterostructure. This architecture provides an ideal platform for exploiting synergistic plasmonic–photonic interaction, which are anticipated to be the cornerstone of its enhanced antibacterial efficacy.

3.3 Absorbance and zeta potential measurement results

The UV-Vis absorption spectra in Fig. 6 highlight the distinct optical properties imparted by the Au coating. Pristine $\text{Gd}_2\text{O}_3:\text{Eu}^{3+}$ sample exhibits negligible absorption across the visible range (450–750 nm), which is characteristic of its wide bandgap dielectric nature of Gd_2O_3 . In stark contrast, the

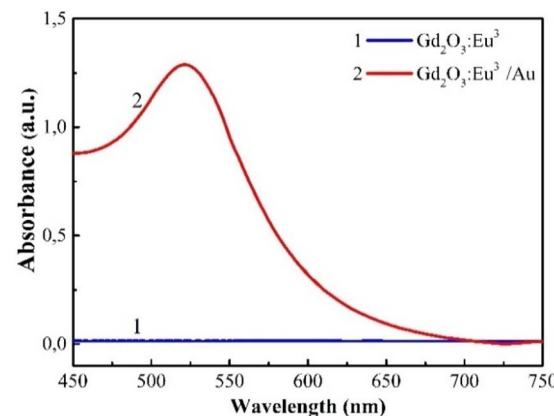


Fig. 6 Absorption spectra of $\text{Gd}_2\text{O}_3:\text{Eu}^{3+}$ and $\text{Gd}_2\text{O}_3:\text{Eu}^{3+}$ /Au samples.

$\text{Gd}_2\text{O}_3:\text{Eu}^{3+}$ /Au nanocomposite displays a pronounced, broad absorption band centered at approximately 525 nm. This feature is a definitive signature of the localized surface plasmon resonance (LSPR) from the deposit of Au NPs, confirming their successful integration and suggesting a potential for significant local electromagnetic field enhancement.

The colloidal stability of the NPs, a critical factor for biomedical applications, was quantified by zeta potential measurement (Fig. 7). The uncoated $\text{Gd}_2\text{O}_3:\text{Eu}^{3+}$ NPs possessed a zeta potential of -15.8 mV, indicating moderate colloidal stability with a tendency to agglomerate. After functionalization with Au, the surface charger shifted dramatically to -74.8 mV, a value that signifies excellent electrostatic stabilization and superior dispersibility in aqueous media. This substantial increase in negative charge is attributed to the combined presence of the polymer stabilizer and the inherently negatively surface charge of the citrate-capped Au NPs.

Collectively, the emergence of a strong LSPR band and the marked shift in zeta potential provide convergent evidence for the successful and homogeneous coating of $\text{Gd}_2\text{O}_3:\text{Eu}^{3+}$ with Au NPs. The enhanced colloidal stability prevents aggregation in

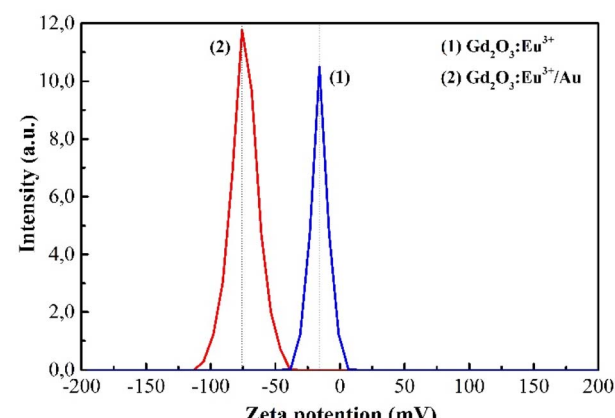


Fig. 7 Zeta potential of $\text{Gd}_2\text{O}_3:\text{Eu}^{3+}$ and $\text{Gd}_2\text{O}_3:\text{Eu}^{3+}$ /Au nano solution samples.



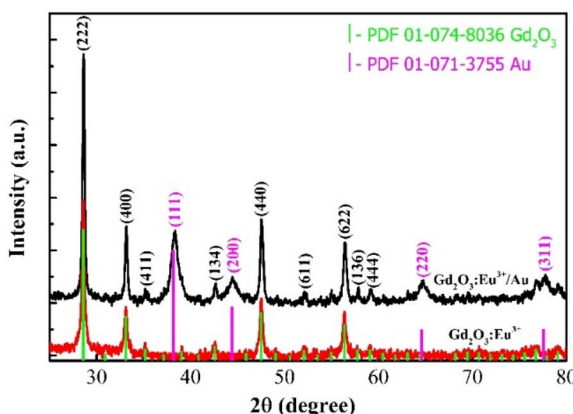


Fig. 8 X-ray diffraction of $\text{Gd}_2\text{O}_3:\text{Eu}^{3+}$ và $\text{Gd}_2\text{O}_3:\text{Eu}^{3+}/\text{Au}$.

biological media, while the plasmon properties establish the foundation for plasmon-enhanced fluorescence collectively contributing to the superior optical and antibacterial performance of the $\text{Gd}_2\text{O}_3:\text{Eu}^{3+}/\text{Au}$ nanocomposite.

3.4 X-ray diffraction results

The crystalline phase and structure purity of the synthesized $\text{Gd}_2\text{O}_3:\text{Eu}^{3+}$ and $\text{Gd}_2\text{O}_3:\text{Eu}^{3+}/\text{Au}$ nanomaterials were characterized by X-ray diffraction (XRD). As present in Fig. 8, the diffraction patterns for both samples are dominated by reflections perfectly indexed to the cubic phase of Gd_2O_3 (PDF 01-074-8036). For the Au-coated sample, additional distinct peaks emerge, corresponding to the (111), (200), (220) and (311) planes of fcc Au (PDF 01-071-3755). The absence of any extraneous diffraction peaks confirms the high phase purity of the synthesized products. The average crystallite size was estimated using the Scherrer equation²⁴ applied to the dominant (222), (400), and (440) reflections of Gd_2O_3 and the (111), (200) reflections of Au. As summarized in Table 1, the calculated crystallite size of the Gd_2O_3 host matrix remains virtually unchanged after Au functionalization, indicating that the deposition process does not induce significant sintering or structural degradation. The observed discrepancy between the crystallite size derived from the XRD analysis and the significantly larger particle size (~ 80 nm) obtained *via* HRTEM observation is a direct consequence of the material's polycrystalline nature. Specifically, the size calculated from the Scherrer equation represents the average dimension of the coherently diffracting domains (*e.g.* the constituent primary crystallites), whereas the size observed by HRTEM corresponds to the physical dimension of the secondary particles or

Table 1 Crystalline size of $\text{Gd}_2\text{O}_3:\text{Eu}^{3+}$ sample

Samples	Crystal size (nm)	
	Gd_2O_3	Au
$\text{Gd}_2\text{O}_3:\text{Eu}^{3+}$	37.83	—
$\text{Gd}_2\text{O}_3:\text{Eu}^{3+}@\text{Au}$	37.67	8.15

polycrystalline aggregates – which are single entities composed of multiple smaller crystallites bonded together. This aggregation process is primarily driven by the high thermal energy input during the calcination step used to achieve the highly crystalline $\text{Gd}_2\text{O}_3:\text{Eu}^{3+}$ phase and is further influenced by the subsequent surface functionalization and Au-coating processes. This structure is relevant as the overall particle size dictates cellular interaction, while the crystallite size governs the intrinsic luminescence quality.

3.5 Raman measurement results

Raman spectroscopy under 785 nm excitation was employed to probe the phonon structure of the Gd_2O_3 lattice (Fig. 9a). The spectrum of the $\text{Gd}_2\text{O}_3:\text{Eu}^{3+}$ sample displays the characteristic vibrational modes of the cubic phase. The weak low-frequency bands at ~ 174 and 220 cm^{-1} (Ag) are assigned to Gd–O bending vibrations. The more prominent features at 300, 318, 360, and 440 cm^{-1} (of Fg, Ag symmetry) are attributed to lattice deformation and asymmetric stretching modes. The most intense peak at 360 cm^{-1} (Fg, Ag) is identified as the symmetric Gd–O stretching vibration, a definitive signature of the cubic crystal structure of Gd_2O_3 .²⁵ A weaker band at $\sim 570\text{ cm}^{-1}$ (Ag) is associated with higher-order O–Gd–O vibrational mode. The absence of peak shift or extra modes confirms that Eu^{3+} doping does not perturb the host lattice, consistent with isovalent substitution of Gd^{3+} by Eu^{3+} ions.

Under 532 nm excitation, the spectrum is dominated by sharp intra-4f emission lines from the Eu^{3+} activator ions (Fig. 9b). The observed bands in the 580–708 nm range correspond to the ${}^5\text{D}_0 \rightarrow {}^7\text{F}_j$ ($j = 0\text{--}4$) transitions. The pronounced intensity of the electric-dipole-dominated ${}^5\text{D}_0 \rightarrow {}^7\text{F}_2$ transition, relative to the magnetic dipole ${}^5\text{D}_0 \rightarrow {}^7\text{F}_1$ transition, indicates that the Eu^{3+} ions occupy lattice sites with low local inversion symmetry in the Gd_2O_3 lattice. In this resonant excitation regime, the efficient direct population of the Eu^{3+} 4f states results in intense luminescence that overwhelms the weaker Raman scattering from the lattice.

A critical observation is – the significant quenching of the Eu^{3+} emission intensity in the $\text{Gd}_2\text{O}_3:\text{Eu}^{3+}/\text{Au}$ composite which is directly related to the pronounced reduction in emission intensity across the entire spectral range. This quenching effect can be explained by plasmon-induced absorption and scattering from Au NPs, together with the introduction of additional non-radiative energy transfer from the excited Eu^{3+} ions to the Au NPs and relaxation pathways, facilitated by the overlapping Au plasmon resonance. While the Au coating enhances multi-functional properties such as catalytic and antibacterial performance, competing process in this composites such as plasmon-induced scattering and the introduction of new non-radiative decay channels at the metal–oxide interface also contribute to the reduced luminescence yield. This illustrates a fundamental trade-off in such hybrid systems: the incorporation of plasmonic Au enhances functionalities like photocatalytic and antibacterial activity but at the expense of luminescence efficiency due to parasitic quenching. The design

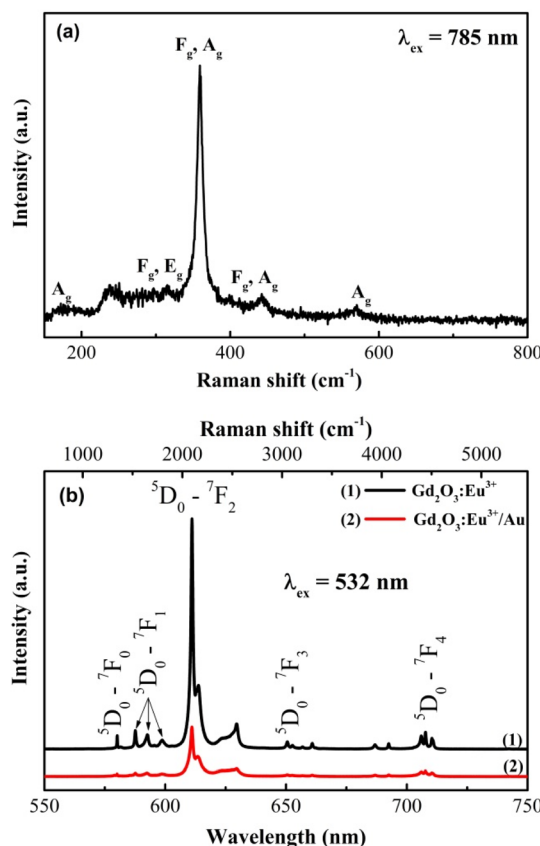


Fig. 9 Raman spectra of (a) $\text{Gd}_2\text{O}_3:\text{Eu}^{3+}$ and (b) $\text{Gd}_2\text{O}_3:\text{Eu}^{3+}/\text{Au}$.

of these $\text{Gd}_2\text{O}_3:\text{Eu}^{3+}/\text{Au}$ composites must therefore be optimized to balance these opposing effects for the intended application.

3.6 FT-IR results

The FTIR spectra of PEI, $\text{Gd}_2\text{O}_3:\text{Eu}^{3+}$, and the $\text{Gd}_2\text{O}_3:\text{Eu}^{3+}/\text{Au}$ hybrid are presented in Fig. 9. For the pristine $\text{Gd}_2\text{O}_3:\text{Eu}^{3+}$ host, the strong absorption band centered around 539 cm^{-1} is characteristic of Gd–O/Eu–O stretching vibration, confirming the successful formation of the cubic lanthanide oxide lattice.

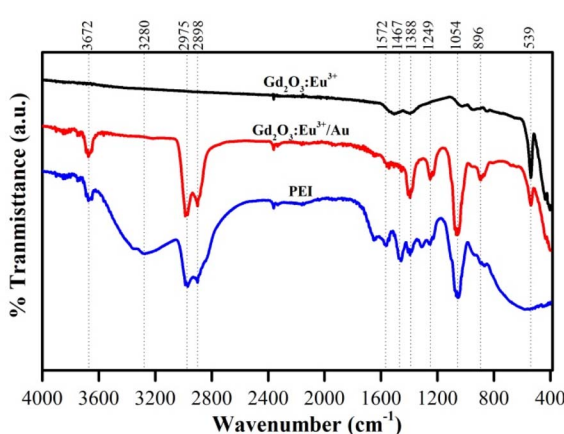


Fig. 10 FTIR spectra of $\text{Gd}_2\text{O}_3:\text{Eu}^{3+}$, $\text{Gd}_2\text{O}_3:\text{Eu}^{3+}/\text{Au}$ and PEI.

The weaker bands observed at 896 and 1054 cm^{-1} are typically associated with residual C–O stretching or M–O–M bending modes within the oxide framework. In the spectrum of the final $\text{Gd}_2\text{O}_3:\text{Eu}^{3+}/\text{Au}$ hybrid, the appearance of new, distinct absorption peaks at 1572 cm^{-1} (–N–H bending), 1467 cm^{-1} (–CH₂ bending), 1249 cm^{-1} and 1054 cm^{-1} (C–N stretching) provides unequivocal evidence for the successful anchoring of polyethyleneimine (PEI) onto the $\text{Gd}_2\text{O}_3:\text{Eu}^{3+}$ surface prior to Au deposition. PEI thus serves as an essential intermediate layer, supplying the primary amine groups for the subsequent coordination-based anchoring of the Au NPs. Moreover, the slight shifts and changes in the relative intensity of the PEI characteristic peaks in the Au-coated sample (relative to pure PEI reference) suggest the existence of weak interactions between the amino functional groups of the PEI coating and the deposited Au NPs. Critically, the weak residual intensity of the PEI signals overall confirm the effective removal of unbound polymer during the washing process, minimizing potential cytotoxic influence and ensuring the biocompatibility necessary for antimicrobial applications (Fig. 10).

3.7 Photoluminescence excitation and emission properties

The photoluminescence properties of $\text{Gd}_2\text{O}_3:\text{Eu}^{3+}$ and $\text{Gd}_2\text{O}_3:\text{Eu}^{3+}/\text{Au}$ samples were investigated through photoluminescence excitation (PLE) and emission (PL) spectroscopy.

The photoluminescence excitation (PLE) spectrum of $\text{Gd}_2\text{O}_3:\text{Eu}^{3+}$, monitored at the dominant 611 nm emission (${}^5\text{D}_0 \rightarrow {}^7\text{F}_2$), is presented in Fig. 11a. The most prominent feature is a broad, intense band centered at 256 nm (spanning 230 – 280 nm), which is unequivocally assigned to the charge transfer band (CTB) from the O^{2-} ligands to the Eu^{3+} center.²⁶ This CTB represents the most efficient excitation pathway for populating the Eu^{3+} emitter. A series of weaker bands in the 270 – 320 nm range are identified as the (${}^8\text{S}_{7/2} \rightarrow {}^6\text{I}_j$) transitions of the Gd^{3+} sublattice, confirming an effective $\text{Gd}^{3+} \rightarrow \text{Eu}^{3+}$ energy transfer cascade, wherein the Gd^{3+} ions act as sensitizing antennas. Furthermore, the sharp lines in the 350 – 500 nm region originate from direct intra-4f excitations of Eu^{3+} , with the characteristic ${}^7\text{F}_0 \rightarrow {}^5\text{L}_6$ (395 nm) and ${}^7\text{F}_0 \rightarrow {}^5\text{D}_2$ (465 nm) transitions being clearly resolved.²⁷

The corresponding photoluminescence emission (PL) spectra under both CTB excitation (250 nm) and direct ${}^7\text{F}_0 \rightarrow {}^5\text{L}_6$ excitation (395 nm) are presented in Fig. 11b. In both cases, the spectra are dominated by the characteristic red emission from the ${}^5\text{D}_0$ excited state of Eu^{3+} , featuring transitions to the ${}^7\text{F}_j$ ($j = 0$ – 4) manifold. The emission lines are observed at approximately 580 nm (${}^5\text{D}_0 \rightarrow {}^7\text{F}_0$), 592 nm (${}^5\text{D}_0 \rightarrow {}^7\text{F}_1$), 611 nm (${}^5\text{D}_0 \rightarrow {}^7\text{F}_2$), 650 nm (${}^5\text{D}_0 \rightarrow {}^7\text{F}_3$), and 705 nm (${}^5\text{D}_0 \rightarrow {}^7\text{F}_4$). The electric-dipole dominated ${}^5\text{D}_0 \rightarrow {}^7\text{F}_2$ transition at 611 nm is the most intense, consistent with the Eu^{3+} ions occupying low-symmetry, non-centrosymmetric sites in the host lattice. While the overall emission intensity is significantly higher under CTB excitation due to its superior absorption cross-section, the efficient direct f–f excitation at 395 nm still produces strong red luminescence. This demonstrates the material's versatility of the $\text{Gd}_2\text{O}_3:\text{Eu}^{3+}$ system, being effectively

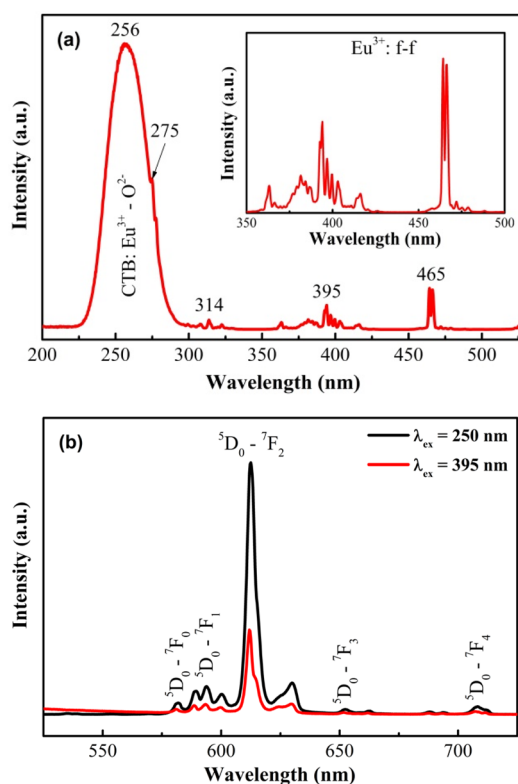


Fig. 11 Photoluminescence spectra of $\text{Gd}_2\text{O}_3:\text{Eu}^{3+}$ nanocrystals: excitation spectra (a); emission spectra (b).

excited *via* both indirect (host sensitized) and direct activator pathways.

Similarly, the PLE spectrum of the $\text{Gd}_2\text{O}_3:\text{Eu}^{3+}/\text{Au}$ nanocomposite, monitored at 611 nm (Fig. 12a), reveals that the fundamental excitation channels remain intact post-functionalization. A broad band in the 230–280 nm range, peaking at 250 nm, is assigned to the $\text{Eu}^{3+}-\text{O}^{2-}$ charge transfer band (CTB). The spectrum also retains signatures of the Gd^{3+} sensitization pathway (${}^3\text{S}_{7/2} \rightarrow {}^6\text{I}_1$ transitions in the 270–320 nm region) and characteristic intra-4f excitation of Eu^{3+} , most notably the ${}^7\text{F}_0 \rightarrow {}^5\text{L}_6$ (~395 nm) and ${}^7\text{F}_0 \rightarrow {}^5\text{D}_2$ (~465 nm) transitions. This confirms the continued coexistence of CTB

absorption, $\text{Gd}^{3+} \rightarrow \text{Eu}^{3+}$ energy transfer, and direct intra-4f excitations of Eu^{3+} in the hybrid system.

The corresponding emission spectra under both 250 nm (CTB) and 395 nm (f-f) excitations are shown in Fig. 12b. The characteristic ${}^5\text{D}_0 \rightarrow {}^7\text{F}_j$ ($j = 0-4$) transitions of Eu^{3+} are clearly observed, with the electric-dipole-dominated ${}^5\text{D}_0 \rightarrow {}^7\text{F}_1$ transition at 611 nm remaining the most intense, preserving the material's red emission profile. However, a direct comparison with the pristine material (Fig. 10b) reveals a substantial quenching of the overall luminescence intensity.

This pronounced attenuation is attributed to efficient non-radiative energy transfer from the excited Eu^{3+} ions to the Au NPs, a process driven by the spectral overlap between the Eu^{3+} emission and the Au localized surface plasmon resonance (LSPR) in the visible region (520–550 nm). The plasmonic nanostructures introduce competing decay channels, including intensified scattering and absorption, which effectively depopulate the ${}^5\text{D}_0$ state and suppress radiative emission. This demonstrates a strong plasmon-fluorophore interaction between the Eu^{3+} emitting centers and the Au NPs, where the quenching mechanism dominates over any potential enhancement hence highlighting the plasmon-mediated modulation of the optical properties in such hybrid system. These findings underscore that the optical output of such hybrid systems is a sensitive function of the plasmonic architecture. By strategically engineering parameters such as the size, density, and spatial distribution of Au NPs, it may be possible to shift the balance from the observed quenching regime to a plasmon-enhanced fluorescence regime. This offers a versatile design principle for tailoring multifunctional nanomaterials for specific applications in bioimaging, sensing, or active plasmonic devices.

3.8 Photoluminescence excitation and emission properties

The fluorescence decay profiles of the $\text{Gd}_2\text{O}_3:\text{Eu}^{3+}$ and $\text{Gd}_2\text{O}_3:\text{Eu}^{3+}/\text{Au}$ (Fig. 13) were recorded by monitoring the characteristic ${}^5\text{D}_0 \rightarrow {}^7\text{F}_2$ hypersensitive transition ($\lambda_{\text{em}} = 611$ nm) under 256 nm excitation. The decay kinetics for both samples were accurately modelled using a bi-exponential function:

$$I = A_1 \exp(-t/\tau_1) + A_2 \exp(-t/\tau_2)$$

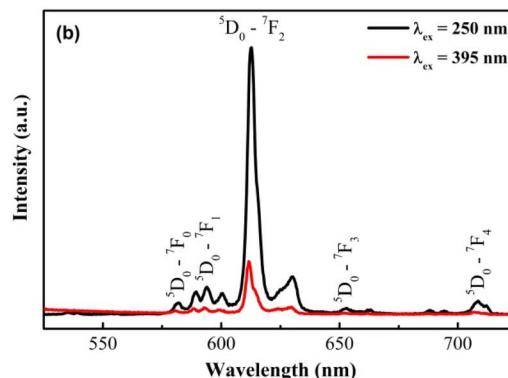
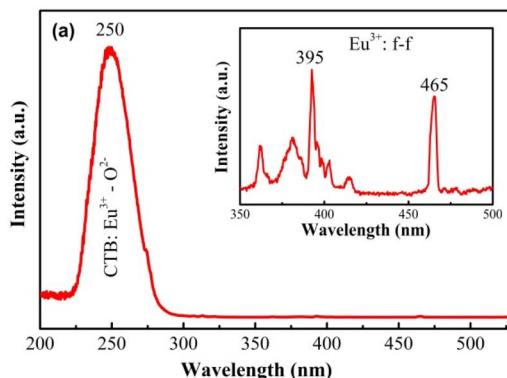


Fig. 12 Luminescent spectra of $\text{Gd}_2\text{O}_3:\text{Eu}^{3+}/\text{Au}$ nanocrystals: excitation spectra (a); emission spectra (b).

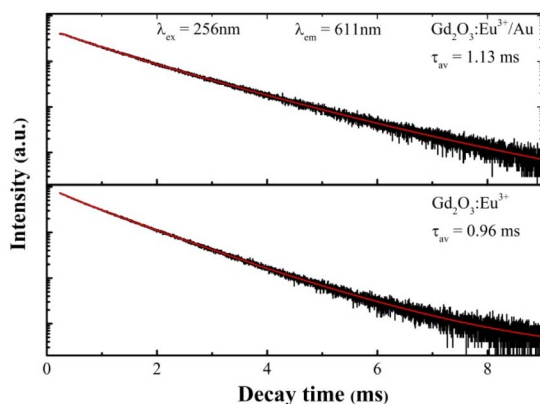


Fig. 13 Fluorescence decay curves of $\text{Gd}_2\text{O}_3:\text{Eu}^{3+}$ and $\text{Gd}_2\text{O}_3:\text{Eu}^{3+}/\text{Au}$.

where, $I(t)$ is the emission intensity at time t . τ_1 and τ_2 are the lifetimes of the short and long decay components, respectively, and A_1, A_2 are their corresponding pre-exponential factors. The average lifetime (τ_{avg}) was then calculated using the standard formula:

$$\tau_{\text{avg}} = \frac{\sum (A_i \times \tau_i)}{\sum A_i}$$

Both curves are well described by a bi-exponential function, indicating that the emission primarily arises from the radiative

Table 2 Decay time fitting parameters and average fluorescence lifetimes of $\text{Gd}_2\text{O}_3:\text{Eu}^{3+}$ and $\text{Gd}_2\text{O}_3:\text{Eu}^{3+}/\text{Au}$

	$\text{Gd}_2\text{O}_3:\text{Eu}^{3+}$	$\text{Gd}_2\text{O}_3:\text{Eu}^{3+}/\text{Au}$
A_1	2.171	2.480
τ_1 (ms)	0.397	1.130
A_2	7.703	2.480
τ_2 (ms)	1.023	1.130
Average lifetime (ms)	0.96	1.13
Goodness of fit (R^2)	0.9997	0.9990

Table 3 Characteristics of 5 bacterial strains

Microorganism	ATCC code	Gram	Morphology & size	Biochemical characteristics	Research significance
<i>Escherichia coli</i>	25922	Negative	Rod-shaped, $1\text{--}3 \times 0.4\text{--}0.7 \mu\text{m}$, motile	Lactose fermentation, oxidase (–), Standard Gram-negative strain for catalase (+)	Antibiotic susceptibility testing and antimicrobial evaluation
<i>Staphylococcus aureus</i>	25923	Positive	Cocci, $0.5\text{--}1.5 \mu\text{m}$, arranged in clusters	Catalase (+), coagulase (+), mannitol fermentation	Standard Gram-positive strain, representative of pathogenic bacteria
<i>Klebsiella pneumoniae</i>	700603	Negative	Rod-shaped, $1\text{--}2 \times 0.5\text{--}0.8 \mu\text{m}$, non-motile, thick capsule	Lactose fermentation, urease (+), oxidase (–)	Gram-negative capsulated bacterium with high antibiotic resistance
<i>Pseudomonas aeruginosa</i>	27853	Negative	Rod-shaped, $1.5\text{--}3 \times 0.5\text{--}0.8 \mu\text{m}$, motile with single polar flagellum	Oxidase (+), catalase (+), produces pyocyanin pigment	Highly drug-resistant Gram-negative bacterium, common in hospital-acquired infections
<i>Candida albicans</i>	14053	— (Yeast)	Yeast cells $2\text{--}6 \mu\text{m}$, capable of forming pseudohyphae and true hyphae	Ferments and assimilates glucose, maltose, sucrose	Pathogenic yeast strain used for antifungal activity evaluation



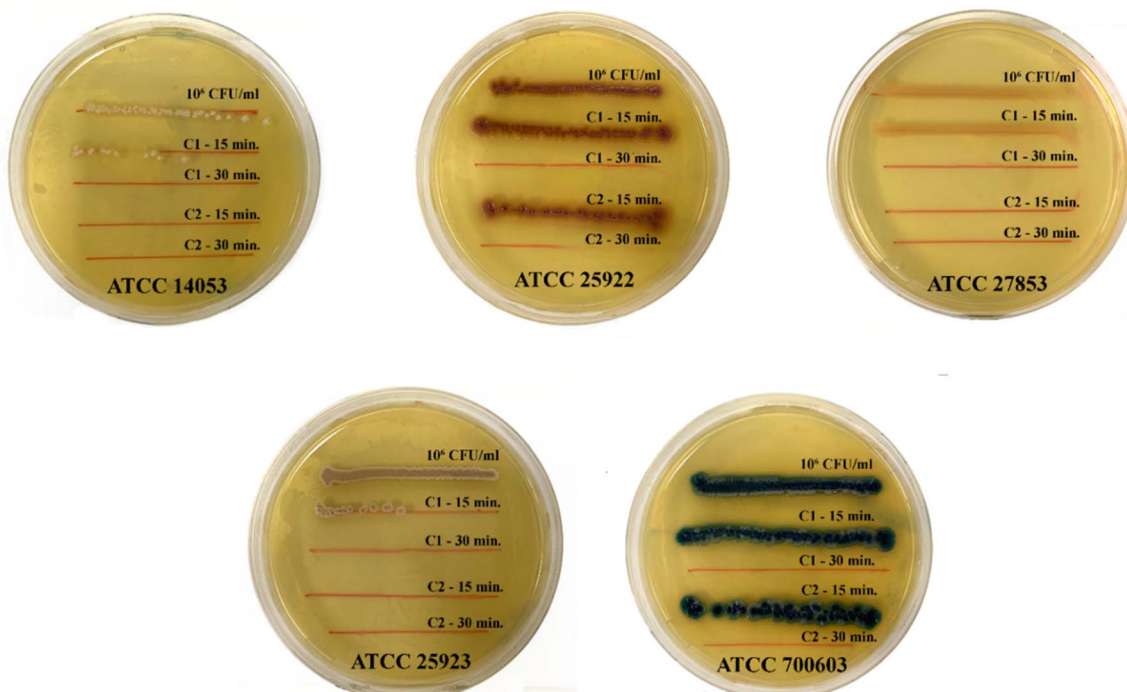


Fig. 14 Antibacterial results of solution 1 (C1) – $\text{Gd}_2\text{O}_3:\text{Eu}^{3+}$ (10 mg ml^{-1}) and solution 2 (C2) – $\text{Gd}_2\text{O}_3:\text{Eu}^{3+}/\text{Au}$ (10 mg ml^{-1}) in 15 minutes and 30 minutes.

aureus), and the chitinous cell wall of fungal pathogens like *C. albicans*.^{28–30}

For *C. albicans*, the Au-coated nanomaterials can interact with the cell membrane and cell wall components (e.g., β -glucans, mannoproteins), impairing key virulence factors, such as the adhesion proteins and morphogenetic transitions essential for its pathogenicity. Under optical excitation, the Au component significantly drives the enhanced antimicrobial activity *via* its LSPR effect. The excited plasmons can induce localized heating *via* the photothermal effect and may also promote the generation of reactive oxygen species (ROS) through plasmon-assisted photocatalytic processes.³¹ Furthermore, the $\text{Gd}_2\text{O}_3:\text{Eu}^{3+}$ oxide host could contribute to this response by facilitating energy transfer or charge separation. Collectively, the combined effects of the hybrid nanostructure – membrane disruption, localized heating, and possible ROS generation – lead to a synergistic antimicrobial mechanism effective against diverse microbial strains.

4 Conclusions

In summary, we have successfully synthesized well-defined $\text{Gd}_2\text{O}_3:\text{Eu}^{3+}$ nanospheres and their Au coated $\text{Gd}_2\text{O}_3:\text{Eu}^{3+}$ nanomaterials *via* a facile multistep route. Their structural features, optical properties, and antibacterial activities were comprehensively investigated. The results reveal the cubic phase of the host matrix $\text{Gd}_2\text{O}_3:\text{Eu}^{3+}$ with the homogeneous distribution of sub-10 nm Au NPs on the surface without perturbing the host crystal structure. FTIR analysis verifies the successful surface functionalization by PEI and the subsequent

attachment of Au nanoparticles. The Au coating introduced a distinct localized surface plasmon resonance (LSPR), as verified by UV-Vis and Raman spectroscopy, and significantly enhanced the colloidal stability, a critical factor for biological applications. The detailed excitation, emission, and fluorescence lifetime measurements definitively established the characteristic ${}^5\text{D}_0 \rightarrow {}^7\text{F}_j$ radiative transitions of Eu^{3+} and revealed a pronounced prolongation of the lifetime after Au deposition. This critical kinetic evidence confirms the successful plasmon-mediated modulation of the Eu^{3+} radiative pathway, enhancing the luminescence efficiency. Furthermore, *in vitro* antimicrobial assays demonstrate that the $\text{Gd}_2\text{O}_3:\text{Eu}^{3+}/\text{Au}$ hybrid exhibits significantly enhanced antimicrobial performance against targeted microbial strains compared to the $\text{Gd}_2\text{O}_3:\text{Eu}^{3+}$ pristine host. The successful integration of Eu^{3+} luminescent centers with the Au LSPR effect yields a truly multifunctional nanomaterial that combines distinctive optical properties with superior biological activity. The observed enhancement in antimicrobial performance suggests a synergistic mechanism driven by hybrid architecture. This novel architecture holds immense promise for next generation applications in plasmon-enhanced biosensing, high-resolution bioimaging, and sophisticated light-assisted antimicrobial and theranostic treatments.

Author contributions

All authors made significant contributions to this study. Nguyen Thanh Huong conceived the research idea, designed the experiments, supervised the project, and prepared the original



draft. Pham Thi Lien carried out material synthesis and data processing. Hoang Thi Khuyen conducted antibacterial assays and interpreted the results. Nguyen Thi Ngoc Anh analysed the data and revised the manuscript. Do Khanh Tung performed structural characterizations and analysed the results. Nguyen Vu conducted optical measurements and data analysis. Lam Thi Kieu Giang performed TEM/SEM measurements and image analysis. Dinh Manh Tien carried out Raman and UV-Vis analyses and assisted with references. Nguyen Thanh Binh co-supervised the work and contributed to manuscript editing.

Conflicts of interest

The authors declare that they have no conflicts of interest.

Data availability

All data are presented in the article. All data generated and analyzed during the current study are available within this manuscript.

Acknowledgements

This research is funded by Vietnam Academy of Science and Technology, under grant number KHCBL.02/23-24. The authors gratefully acknowledge the Laboratory of Photochem, Photonics and Imaging and the National Key Laboratory for Electronic Materials and Devices, Institute of Materials Science, for their support. Thanks to the Laboratory of Vietnam Military Medical University and 108 Military Central Hospital for creating conditions for conducting experiments and measurements.

References

- 1 V. Bedekar, D. P. Dutta, M. Mohapatra, S. V. Godbole, R. Ghildiyal and A. K. Tyagi, Rare-earth doped gadolinium based phosphors for potential multicolor and white light emitting deep UV LEDs, *Nanotechnology*, 2009, **20**(12), 125707.
- 2 G. Xing, O. Guo, Q. Liu, Y. Li, Y. Wang, Z. Wu and G. Wu, Highly uniform $\text{Gd}(\text{OH})_3$ and $\text{Gd}_2\text{O}_3:\text{Eu}^{3+}$ hexagram-like microcrystals: glucose-assisted hydrothermal synthesis, growth mechanism and luminescence property, *Ceram. Int.*, 2014, **40**(5), 6569–6577.
- 3 S. Singh, S. P. Khatkar, D. Kumar and V. B. Taxak, Synthesis and optical properties of $\text{Gd}_{2(1-x)}\text{O}_3: 2x\text{Eu}^{3+}$ nanophosphors via tartaric assisted sol-gel route, *J. Sol-Gel Sci. Technol.*, 2015, **74**(1), 24–31.
- 4 T. K. Anh, N. T. Huong, P. T. Lien, D. K. Tung, V. D. Tu, N. D. Van, W. Strek and L. Q. Minh, Great enhancement of monodispersity and luminescent properties of $\text{Gd}_2\text{O}_3:\text{Eu}$ and $\text{Gd}_2\text{O}_3:\text{Eu}$ @ silica nanospheres, *Mater. Sci. Eng., B*, 2019, **241**, 1–8.
- 5 R. Priya and O. P. Pandey, Hydrothermal synthesis of Eu^{3+} -doped Gd_2O_3 nanophosphors and its Judd-Ofelt analysis, *Vacuum*, 2018, **156**, 283–290.
- 6 N. Vu, N. K. K. Minh, T. T. D. Hien, P. D. Roan, L. T. K. Giang, N. T. Huong, H. T. Khuyen, P. T. Lien, D. M. Tien, N. T. Kien and D. N. Nghiem, Structure, morphology, optical properties, and Judd-Ofelt analysis of $\text{Y}_{(1-x)}\text{V}_x\text{O}_4:\text{Eu}^{3+}$ materials synthesized by the combustion method, *Nanoscales Adv.*, 2025, **7**(13), 4077.
- 7 D. A. Zatsepin, D. W. Boukhvalov, A. F. Zatsepin, Y. A. Kuznetsova, M. A. Mashkovtsev, V. N. Rychkov, V. Y. Shur, A. A. Esin and E. Z. Kurmaev, Electronic structure, charge transfer, and intrinsic luminescence of gadolinium oxide nanoparticles: Experiment and theory, *Appl. Surf. Sci.*, 2018, **436**, 697–707.
- 8 P. T. Lien, V. D. Tu, L. N. Diep, N. T. Huong, H. T. Khuyen, N. T. N. Anh, V. X. Nghia, T. K. Anh, R. Tomala and L. Q. Minh, Characterization of $\text{Gd}_2\text{O}_3:\text{Eu}^{3+}$ Nanocomplexes Conjugate with IgG for the Identification of CEA Tumor Cells, *Mater. Trans.*, 2020, **61**(8), 1575–1579.
- 9 H. Deng, F. Chen, C. Yang, M. Chen, L. Li and D. Chen, Effect of Eu doping concentration on fluorescence and magnetic resonance imaging properties of $\text{Gd}_2\text{O}_3:\text{Eu}^{3+}$ nanoparticles used as dual-modal contrast agent, *Nanotechnology*, 2018, **29**, 415601.
- 10 S. Chaudhary, S. Kumar, A. Umar, J. Singh, M. Rawat and S. K. Mehta, Europium-doped gadolinium oxide nanoparticles: A potential photoluminescent probe for highly selective and sensitive detection of Fe^{3+} and Cr^{3+} ions, *Sens. Actuators, B*, 2017, **243**, 579–588.
- 11 R. Priya, M. Michalska-Domańska, S. Kumar and O. P. Pandey, Morphological and optical studies of $\text{Gd}_2\text{O}_3:\text{Eu}$ nanostructures synthesized via sacrificial template directed co-precipitation route, *Opt. Laser Technol.*, 2021, **143**, 107357.
- 12 N. T. Huong, D. T. Thao, N. T. Nghia, N. T. Nga, P. T. Lien, H. T. Phuong, N. V. Nghia, V. Duong, T. T. Huong, T. K. Anh and L. Q. Minh, Optic bionanospherical probe from Gd_2O_3 : Yb, Er upconverting nanosphere and mAb⁺CD133 antibody for precise imaging label of cancer stem cell NTERA-2, *Commun. Phys.*, 2023, **33**(3), 253.
- 13 S. K. Ranjan, M. Mondal and V. K. Rai, $\text{Er}^{3+}\text{-Yb}^{3+}/\text{Er}^{3+}\text{-Yb}^{3+}\text{-Li}^{+}/\text{Er}^{3+}\text{-Yb}^{3+}\text{-Zn}^{2+}$: Gd_2O_3 nanophosphors for efficient frequency upconverter and temperature sensing applications, *Mater. Res. Bull.*, 2018, **106**, 66–73.
- 14 W. Zhang, Z. Huang, X. Pu, X. Chen, G. Yin, L. Wang, F. Zhang and F. Gao, Fabrication of doxorubicin and chlorotoxin-linked Eu- Gd_2O_3 nanorods with dual-modal imaging and targeted therapy of brain tumor, *Chin. Chem. Lett.*, 2020, **31**(1), 285–291.
- 15 N. R. Nadar, J. Deepak, S. C. Sharma, B. R. Radha Krushna, Puneeth, R. Sowjanya, V. Sureka Varalakshmi, S. Sahu, B. Sargunam, H. Nagabhushana, B. E. Kumar Swamy and S. S. Ruthwik, Graphene oxide based $\text{Gd}_2\text{O}_3:\text{Eu}^{3+}$ nanocomposites: A multifaceted approach to advanced energy storage and bio sensing applications, *Inorg. Chem. Commun.*, 2024, **165**, 112515.
- 16 R. Priya, O. P. Pandey and S. J. Dhoble, Review on the synthesis, structural and photo-physical properties of



Gd₂O₃ phosphors for various luminescent applications, *Opt Laser Technol.*, 2021, **135**, 106663.

17 G.-Y. Yao, Q.-L. Liu and Z.-Y. Zhao, Studied Localized Surface Plasmon Resonance Effects of Au Nanoparticles on TiO₂ by FDTD Simulations, *Catalysts*, 2018, **8**, 236.

18 M. Xu, L. Nahar, K. J. Ritchie, C. Wang, L. Cheng, Z. Wu, S. D. Sarker and M. Guo, Recent advances in nanomaterial-based optical biosensors and their biomedical and biopharmaceutical applications, *J. Pharm. Anal.*, 2025, 101349.

19 L. Xiao, X. Tian, S. Harihar, Q. Li, L. Li, D. R. Welch and A. Zhou, Gd₂O₃-doped silica @ Au nanoparticles for *in vitro* imaging cancer biomarkers using surface-enhanced Raman scattering, *Spectrochim. Acta, Part A*, 2017, **181**, 218–225.

20 J. Yang, Q. Zhao, Z. Zang, S. Zhang, Z. Wang, L. Li, X. Yu, X. Yang, Z. Lu and X. Zhang, A dual-mode T1 MRI/CT contrast agent of Gd₂O₃/Au@MSNs for tumor imaging with high performance, *Materialia*, 2022, **24**, 101494.

21 I. J. Lithi, K. I. A. Nakib, A. M. S. Chowdhury and M. S. Hossain, A review on the green synthesis of metal (Ag, Cu, and Au) and metal oxide (ZnO, MgO, Co₃O₄, and TiO₂) nanoparticles using plant extracts for developing antimicrobial properties, *Nanoscale Adv.*, 2025, **7**(9), 2446–2473.

22 M. K. Verma, M. D. Bala, P. B. Khoza, T. R. Papo and M. L. Shozi, Core–shell nanoparticles for water purification: Advances in photocatalytic and antimicrobial applications, *Next Mater.*, 2025, **9**, 101186.

23 D. Téllez-de-Jesús, N. S. Flores-Lopez, J. A. Cervantes-Chávez and A. R. Hernández-Martínez, Antibacterial and antifungal activities of encapsulated Au and Ag nanoparticles synthesized using *Argemone mexicana* L. extract, against antibiotic-resistant bacteria and *Candida albicans*, *Surf. Interfaces*, 2021, **27**, 101456.

24 S. A. Hassanzadeh-Tabrizi, Precise calculation of crystallite size of nanomaterials: A review, *J. Alloys Compd.*, 2023, **968**, 171914.

25 E. V. Silina, N. E. Manturova, E. L. Chuivilina, A. A. Gasanov, O. I. Andreeva, M. A. Pugachevskii, A. V. Kochura, A. A. Kryukov, Y. G. Suzdaltseva and V. A. Stupin, Biomedical Application Prospects of Gadolinium Oxide Nanoparticles for Regenerative Medicine, *Pharmaceutics*, 2024, **16**, 1627.

26 A. Jain, G. A. Hirata, M. H. Farias and F. F. Castillón, Synthesis and characterization of (3-aminopropyl) trimethoxy-silane (APTMS) functionalized Gd₂O₃:Eu³⁺ red phosphor with enhanced quantum yield, *Nanotechnology*, 2016, **27**(6), 65601.

27 W. U. Yanli, X. U. Xianzhu, L. I. Qianlan, Y. Ruchun, D. Haixin and X. Qiang, Synthesis of bifunctional Gd₂O₃:Eu³⁺ nanocrystals and their applications in biomedical imaging, *J. Rare Earths*, 2015, **33**(5), 529–534.

28 S. Changra, G. Puri, P. Kumar and S. V. Pawar, Nano-antibiotics: A promising solution to combat antimicrobial resistance in Gram-negative bacteria, *J. Indian Chem. Soc.*, 2025, **102**(10), 102066.

29 X. Chen, L. Lv, J. Xu, J. Shi, X. Chen, G. Zi, Y. Wu, S. Sun, Y. Pang, Q. Song, L. Ma, S. Wei, T. Ma and W. Liu, Au(III) Schiff base complexes as oxidoreductase inhibitors against carbapenem- and colistin-resistant Gram-negative bacteria *via* targeting redox active motifs, *Redox Biol.*, 2025, **86**, 103800.

30 L. Barsé, A. Ulfig, M. Varatnitskaya, M. Vázquez-Hernández, J. Yoo, A. M. Imann, N. Lupilov, M. Fischer, K. Becker, J. E. Bandow and L. I. Leichert, Comparison of the mechanism of antimicrobial action of the gold(I) compound auranofin in Gram-positive and Gram-negative bacteria, *Microbiol. Spectrum*, 2024, **12**(11), 1–24.

31 E. Loscertales, R. López-Méndez, J. Mateo, L. M. Fraile, J. M. Udiás, A. Espinosa and S. España, Impact of gold nanoparticle size and coating on radiosensitization and generation of reactive oxygen species in cancer therapy, *Nanoscale Adv.*, 2025, **7**, 1204–1214.

